Influence of the Atmospheric Surface Layer on a Turbulent Flow Downstream of a Ship Superstructure

LUKSA LUZNIK AND CODY J. BROWNELL

Mechanical Engineering Department, United States Naval Academy, Annapolis, Maryland

MURRAY R. SNYDER

Aerospace Engineering Department, United States Naval Academy, Annapolis, Maryland, and Mechanical and Aerospace Engineering Department, George Washington University, Washington, D.C.

HYUNG SUK KANG

Mechanical Engineering Department, United States Naval Academy, Annapolis, Maryland

(Manuscript received 20 September 2012, in final form 17 March 2013)

ABSTRACT

This paper describes a set of turbulence measurements at sea in the area of high flow distortion in the near-wake and recirculation zone behind a ship's superstructure that is similar in geometry to a helicopter hangar/flight deck arrangement found on many modern U.S. Navy ships. The instrumented ship is a 32-m-long training vessel operated by the United States Naval Academy that has been modified by adding a representative flight deck and hangar structure. The flight deck is instrumented with up to seven sonic anemometers/thermometers that are used to obtain simultaneous velocity measurements at various spatial locations on the flight deck, and one sonic anemometer at bow mast is used to characterize inflow atmospheric boundary conditions. Data characterizing wind over the deck at an incoming angle of 0° (head winds) and wind speeds from 2 to 10 m s^{-1} obtained in the Chesapeake Bay are presented and discussed. Turbulent statistics of inflow conditions are analyzed using the Kaimal universal turbulence spectral model for the atmospheric surface layer and show that for the present dataset this approach eliminates the need to account for platform motion in computing variances and covariances. Conditional sampling of mean flow and turbulence statistics at the flight deck indicate no statistically significant variations between unstable, stable, and neutral atmospheric inflow conditions, and the results agree with the published data for flows over the backward-facing step geometries.

1. Introduction

The flow that forms over a ship superstructure/flight deck geometry is known to generate an unsteady ''air wake'' characterized by recirculation zones just aft of the superstructure and formation of turbulent shear layers at the edges of the hangar superstructure. Significant efforts have been made over the last three decades to gain insight into the air wake around naval vessels (Healey 1987; Zan et al. 1999. The primary purpose of these efforts has been to determine the safe operational envelopes of rotary aircraft, since ship motions combined with air wakes can create potentially hazardous conditions during launch/recovery operations. Presently, aircraft safe operating limits for naval vessels are determined empirically by trials at sea. In addition to being expensive and potentially dangerous to generate, safe operational limits obtained in this way are ship and aircraft configuration specific and are constrained to environmental conditions covered during trials. Given the disadvantages and difficulties in directly obtaining these operational envelopes, researchers and flight test engineers increasingly attempt to rely upon numerical models to gain insight into complex turbulent flows around naval vessels and their impact on the operational envelopes of rotary aircraft. Validations of these computational models are typically made against wind tunnel laboratory

Corresponding author address: Luksa Luznik, Mechanical Engineering Department, United States Naval Academy, 590 Holloway Road, Annapolis, MD 21402.
E-mail: luznik@usna.edu

DOI: 10.1175/JTECH-D-12-00216.1

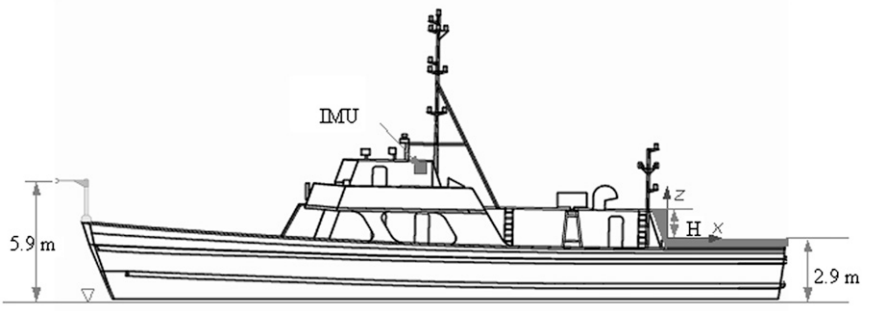

FIG. 1. Schematic of the measurement platform. Hangar, flight deck, and location of reference anemometer are highlighted. Spatial arrangement of anemometers on the flight deck is described in the text.

measurements and as such are limited to Reynolds numbers that are orders of magnitude below those typically observed at full scale. Nevertheless, these studies provide significant insights into air-wake flows as reviewed by Healey (1987, 1992) and more recently by Zan et al. (1999). Major findings include strong dependence of air-wake topology and strength with the flight deck geometry and orientation of the ship to the free stream direction. Recent computational work (Bunnell 2001; Polsky 2003) suggests that atmospheric boundary layers can significantly modify the flow topology over the flight deck and hence, boundary layer effects need to be accounted for in any air-wake model validation effort.

Testing the applicability of air-wake models requires in situ field measurements of the turbulent wake under various well-described environmental forcing conditions. Because field measurements are extremely challenging to obtain, field studies describing air-wake measurements around naval vessels are rare. Wilkinson et al. (1999) describes full-scale trials of British and Australian navies, and Polsky and Bruner (2000) describe in detail a comparison of at-sea measurements with wind tunnel data obtained at the flight deck of a U.S. naval ship. Zan et al. (1999) compare limited full-scale air-wake data with air-wake models and wind tunnel data. Common to these studies are measurements of airflow velocities in the near wake (i.e., measurements in the region directly above the flight deck), with concurrent measurements of ship motions and ship speed, as well as relative wind speed and direction. These studies provided important information about air-wake properties, but they had limited spatial coverage or duration of measurements because of time constrains of ship availability and changing atmospheric characteristics.

At-sea measurements of momentum and heat fluxes from stationary and moving platforms in the context of ocean–atmosphere interaction studies have been well documented. Recently, Miller et al. (2008) and Brooks (2008) provide a review of measurements from various platforms and summarize methods for overcoming problems associated with making high-resolution measurements of turbulence statistics, including bias in flux estimates because of platform motion and flow distortion.

In this paper at-sea measurements of momentum and heat fluxes as well as measurements of flow in the wake of a ship superstructure resembling helicopter hangar/flight deck arrangement are presented and analyzed. It is shown that for the present experiment conducted in the Chesapeake Bay, atmospheric fluxes can be estimated free of ship motion contamination by employing a universal turbulent spectra of the atmospheric surface layer (Kaimal et al. 1972). Furthermore, turbulence statistics and flow topology in the near wake resemble those found in flows behind a backward-facing step. The experimental arrangements are outlined in the following section, with results presented in section 3 and final discussion and conclusions presented in section 4. This work is part of a larger research effort at the United States Naval Academy (USNA) involving comprehensive full-scale measurements and comparing the measurements with model tests in a wind tunnel, both aimed at validating advanced numerical simulations of air wakes over the superstructure of navy ships (Snyder et al. 2011).

2. Methods

a. Measurement platform and instrumentation

Data presented in this paper were collected aboard an instrumented Yard Patrol (YP, training) vessel. The YPs are relatively large vessels with waterline length L_{WL} = 32.9 m and maximum superstructure height, excluding masts, of 7.3 m above the waterline. Figure 1 shows the schematic of the vessel with relevant dimensions indicated.

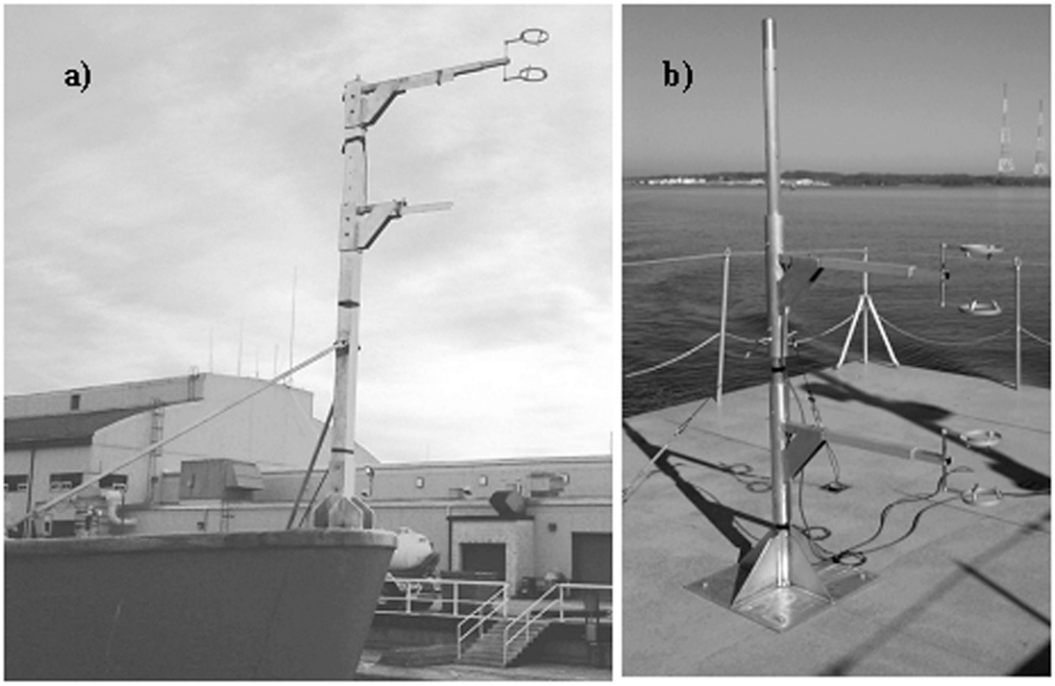

FIG. 2. (a) Bow reference anemometer and (b) anemometer arrangement on the flight deck prior to data collection. The two anemometers shown have sampling volumes at $z = 0.4$ and 0.65 m.

The built-in superstructure resembling a flight deck is 5.7 m long, 6.7 m wide, and the hangar–flight deck geometry resembles a backward-facing step with step height $H = 1.5$ m. The coordinate system used throughout this paper is fixed on the ship fore–aft centerline where the hangar superstructure intersects the flight deck. The positive x direction is aft, positive y is to starboard, and positive z is upward. The reference velocity sensor (see also Fig. 2a), located on the ship's bow 5.9 m above the still waterline, has the same coordinate system and is used to measure incoming flow conditions. The wind over deck direction, referred to as the yaw angle β, is defined as $\beta = \tan^{-1}(v/u)$, where u is x and v is y direction wind velocity. For wind coming from the port side, β is positive and for wind coming from the starboard side it is negative. Figure 1 also shows the location of the inertial measurement unit (IMU) that is used for monitoring the ship's pitch and roll motions during the experiment.

The flight deck is instrumented with an array of velocity sensors attached to vertical masts (see Fig. 2b). Each mast is a 2.5-m-long spar and the number of sensors stacked in the z direction at each (x, y) station during a single run varies from 1 to 3 and can range from $z/H = 0.13$ to 1.4. Thin stainless steel guy wires were added to the masts to improve their rigidity and to eliminate velocity contamination from the ship's structural vibrations. The present measuring system is composed of eight sonic anemometers/thermometers manufactured by Applied Technology Inc. Up to seven anemometers are located on the flight deck and one is permanently used as a reference bow anemometer. All anemometers have "A" type probe configuration (see Figs. 2a,b) measuring three velocity components and sonic temperature. Each anemometer has an internal sampling rate of 200 Hz, and the instrument output sampling rate is user adjustable up to a maximum of 20 Hz. Throughout the experiments, anemometer data output is kept constant at 20 Hz. All eight anemometers are synchronized using a custom-built synchronizer, which in turn is connected to the acquisition computer.

Prior to use in the field experiments, the anemometers were systematically tested in a closed circuit wind tunnel at the USNA (Miklosovic et al. 2011) to estimate directional errors associated with interference with the sensor probe's structural support. Uncertainty in mean velocities was found to lie within $\pm 5\%$ in the range of yaw angles $-90° < \beta < 90°$. Spatial resolution of the anemometers is about 15 cm because of the line averaging over the probe's sonic path (Kaimal et al. 1968). Assuming a characteristic velocity of 3 m s^{-1}, this instrument has a cutoff frequency $f = U/2L$ of 10 Hz, which is considered adequate for the present work. Supporting data collected concurrently with sonic anemometers include continuous measurement of ship's roll and pitch angles using an IMU, and the ship's position and velocity using a Wide Area Augmentation System (WAAS)-enabled

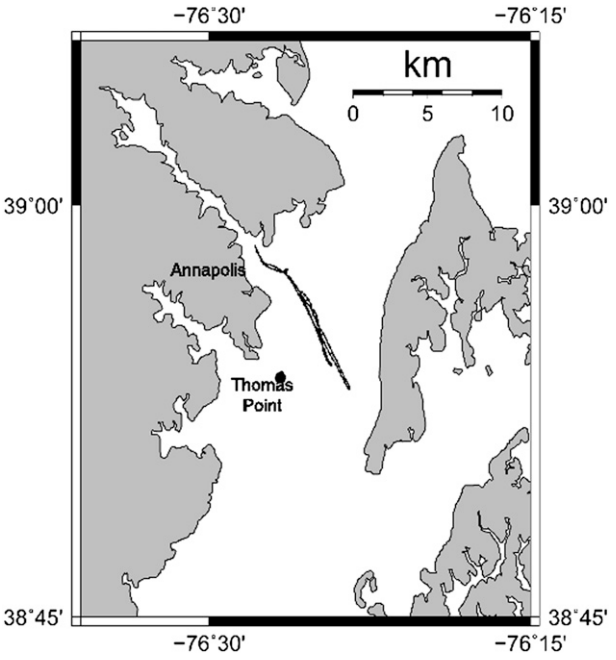

FIG. 3. Map of Chesapeake Bay in the vicinity of the USNA. A sample GPS track of the ship's path during one of the underways is shown. Location of the NOAA Thomas Point meteorological tower is also shown.

GPS with a typical accuracy of 1 m. Local onboard air temperatures and atmospheric pressure are taken at the beginning and end of each data collection period. When available, real-time meteorological data from a nearby fixed meteorological tower are also collected, as described in the following sections.

b. Underway location—Chesapeake Bay

Measurements discussed in this paper were collected over a 1-yr period from March 2010 to March 2011. During this period, we had 12 separate measurement days at sea (called underways) that resulted in 62 datasets for a nominal headwind condition ($\beta = 0°$). All measurements were conducted in the vicinity of the upper Chesapeake Bay estuary in Annapolis, Maryland, as shown in Fig. 3. A sample GPS track of the ship's path during one of the underways is also shown in Fig. 3. On the north side, the measurement area is bounded by the Chesapeake Bay Bridge and on the south by the proximity of the Thomas Point meteorological station, operated and administered by the National Oceanic and Atmospheric Administration (NOAA). Thomas Point meteorological station provides real-time measurements of atmospheric wind speed and direction measured at 18 m above sea level, as well as sea surface temperature, air temperature, and pressure (http://www.ndbc.noaa.gov).

An overview of the atmospheric conditions during the study period is shown in Fig. 4. Wind speed and direction of 10-min averages from Thomas Point tower are shown covering periods from July 2010 to March 2011 (runs 32–62). Data for earlier periods are not available. Wind speed conditions can be qualified as moderate to low, with typical wind speeds of about 4 m s^{-1}, and only on a few occasions did the wind speed exceed 10 m s^{-1} (e.g., runs 36–37 in Fig. 4a). The predominant wind direction is from either the north or south, coinciding with the Chesapeake Bay channel centerline. The resultant mean horizontal relative velocity U_{ref} measured by the reference

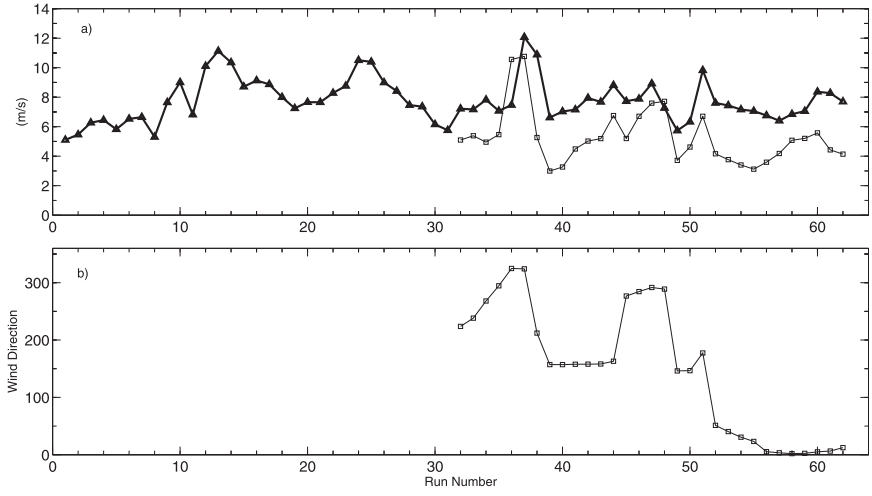

FIG. 4. Ambient wind conditions during study period: (a) The 10-min averages of wind speed from Thomas Point tower (squares) and mean horizontal velocity from the reference anemometer U_{ref} (triangles). (b) The 10-min averages of true wind direction (°) from Thomas Point tower. Note: Thomas Point data for runs 1–31 are not available.

bow anemometer is also shown in Fig. 4a for comparison. Most of the time U_{ref} is larger than the wind speed, with the difference resulting from the ship's speed over ground of about 3 m s^{-1} (6 kt). Details as to how U_{ref} is calculated are described later in the paper.

Characteristics of the surface gravity waves during individual underways were not monitored. However, during the underway corresponding to datasets 32–37, detailed wave information is available from an oceanographic instrument deployed in the vicinity of the measurement area (Luznik and Flack 2010). Significant wave height increased from 0.2 m during ambient wind speed of 5 m s^{-1} to 0.5 m during winds in excess of 10 m s^{-1}. Measured direction of incident waves for both cases coincided with the wind direction from Thomas Point, and wave periods ranged from 2 to 2.5 s, indicating wind-driven waves. These observations are consistent with measurements in the same area by Lin et al. (2002) and show that surface gravity waves in the upper Chesapeake Bay are fetch-limited wind waves with direction coinciding with the prevailing wind direction.

c. Data acquired and anemometer arrangement

For each spatial arrangement of anemometers on the flight deck, data are collected without interruption for approximately 30 min. During data collection a specified target yaw angle (e.g., $\beta = 0°$) and ship speed were maintained as constant as possible. Any deviation from the target ship velocity is accounted for through data postprocessing, as discussed later. The duration of actual obtained measurement periods differ, ranging from as short as 2 min to longer than 40 min because of operational and instrumentation factors. Operational factors include avoiding ship traffic, approaching shallow water, and significantly changing wind direction. In these instances data collection was aborted and if the record length was deemed too short, the run was repeated. Instrumentation factors include excessive data dropout occurrences from one or multiple anemometers within a single dataset. In these instances data collection was aborted and a run was repeated.

To aid in assessment of collected data quality, a real-time monitoring system was used. As the data from all anemometers are continuously streamed from the synchronizer to the acquisition computer, velocity data from the reference anemometer are processed in real time and a time history of temporally averaged (over 15 s) horizontal velocity and yaw angle is displayed in the ship's bridge control room. This information is used to provide real-time data to the helmsman for heading adjustments during the data collection process.

Figure 5 shows the spatial arrangement of anemometer sample volumes in the horizontal (x, y) plane on the flight deck. Coordinates are scaled by hangar height $H = 1.5$ m. As the ship is symmetric in shape, data are sampled predominantly on the starboard side. About 20% of the datasets were collected on the port side of the flight deck, mirroring data from the starboard side. Details of the flight deck anemometer vertical arrangements are not presented here but will be discussed in the results section.

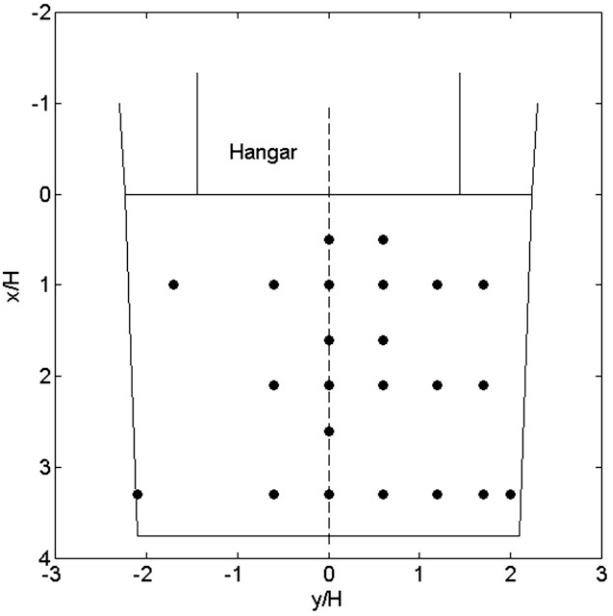

FIG. 5. Spatial arrangement of sonic anemometers in the (x, y) plane on the flight deck. [Adapted from Brownell et al. (2012).]

d. Data analysis

1) CONDITIONAL SAMPLING

Conditional sampling of the reference bow anemometer data for headwind condition ($\beta = 0°$) forms the basis of data selection for further analysis from all anemometers. The process involves identification of time instances from reference anemometer data satisfying the following three criteria: (i) $-10° \le \beta_{filter} \le 10°$, where β_{filter} is a running average over 30 s of instantaneous yaw angle; (ii) continuous record length of data satisfying (i) has to be greater than 30 s; and (iii) instantaneous horizontal velocity u satisfying (i) and (ii) has to be greater than 4 m s^{-1}. Data not satisfying these criteria are discarded for all anemometers. Consequently, data used in the subsequent analysis are not continuous and consist of piecewise data segments longer than 30 s. The longest continuous individual data segment length is just over 30 min and the median is about 3.3 min. A histogram of resulting time-averaged yaw angles, $\langle\beta\rangle$ (where terms in angle brackets indicate the time-averaging operation over an appropriate time scale discussed in the next

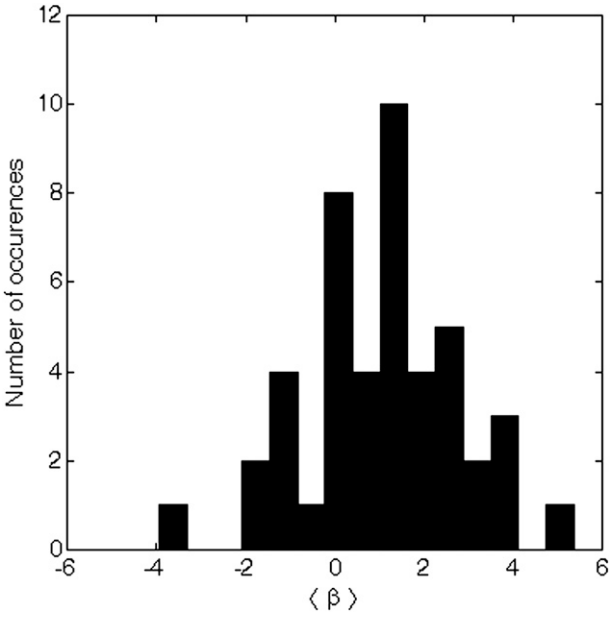

FIG. 6. Histogram of $\langle\beta\rangle$ based on conditionally sampled instantaneous data in the range $-10° \le \beta_{\text{filter}} \le 10°$. Purely headwind conditions $\langle\beta\rangle = 0°$ occurs only in eight datasets.

section), of the conditionally sampled data is presented in Fig. 6. Only eight datasets can be considered a pure headwind condition ($\langle\beta\rangle = 0°$), with combined segment times totaling 210 min. Overall, there is a slight bias toward incoming flow from the port side, that is, positive mean angles with median $\langle\beta\rangle = 1.2°$.

The selection of a 30-s-long low-pass filter that defines β_{filter} was chosen for two reasons. First, the assumption is that yaw angle adjustments are made on a time scale larger than 30 s. This is based on the reasoning that the real-time data display on the bridge is updated every 15 s and that the helmsman is basing the decision to change the ship's heading toward the prevailing wind direction on at least two 15-s updates of the yaw angle. The second reason was to maximize the length of continuous data segments. Brownell et al. (2012) use the same conditional sampling approach as above but with the exception of windowing the yaw angle to $-5° \le \beta \le +5°$. Since most of analyses in this paper are spectrally based, we opted to maximize the length of individual continuous data segments needed for spectral analysis.

2) DATA STATIONARITY

One of the fundamental limitations during any full-scale measurements trying to address turbulence is that ambient atmospheric characteristics are rarely stationary. Consequently, selection of an appropriate averaging time for defining mean velocity and turbulence properties is difficult. In the present experiment, an additional complexity is that the measurements are obtained from a moving platform. Thus, raw anemometer velocities contain not only the time variability of mean ambient wind (at unknown time scale), but also fluctuations resulting from changes in ship speed and direction to maintain desired heading (also at unknown time scale but alluded to it in the previous section to be on the order of 30 s or longer), and ship motions (at 2–3-s time scale) induced by surface gravity waves. Changes in ship speed because of changing magnitude and direction of tidal currents are also present and are not considered an issue since tidal variability is long (roughly 6 h) in comparison to our measurement times.

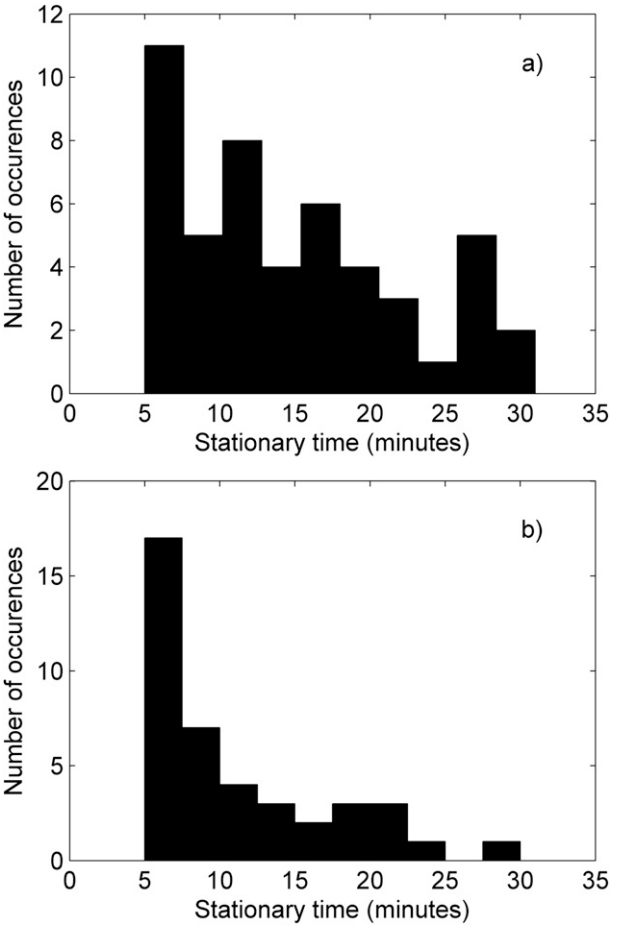

FIG. 7. Histogram of stationary times based on the Bendat and Piersol (1986) run test at 95% confidence level for (a) variance $\langle u'u'\rangle$ and (b) U_{ref}.

To obtain an appropriate averaging period for mean and turbulent quantities, the time series data are examined for stationarity using the run test method (Bendat and Piersol 1986) and following the methodology of Soulsby (1980) by applying a run test to the piecewise data. Outcomes are presented in Figs. 7a and 7b for the

TABLE 1. Summary of the run test (Bendat and Piersol 1986) outcomes at 95% confidence level for quantities of interest. Data are for the reference anemometer.

Quantity	Median stationary time (min)
U_{ref}	10
$\langle u'u' \rangle$	13
$\langle v'v' \rangle$	11
$\langle w'w' \rangle$	13
$-\langle u'w' \rangle$	12

reference anemometer mean relative horizontal velocity U_{ref} and variance $\langle u'u' \rangle$ whereas Table 1 summarizes the stationarity outcomes for all quantities of interest.

Substantial variability in stationary time across datasets is evident in Figs. 7a and 7b for U_{ref} and $\langle u'u' \rangle$. The reason why turbulence statistics have consistently longer stationary records than U_{ref} is a consequence of how the fluctuations (e.g., u', v', and w') are calculated. The fluctuating velocity component is defined by the removal of a linear least squares fit from the instantaneous velocity component over a continuous data segment, and as a result the data improve the stationarity. For 16% of the datasets, a run test could not be applied since they are shorter than the resolution of the run test, which is set to 5 min. This is based on the requirement to have a minimum of 10 consecutive statistically independent estimates of a desired quantity (e.g., mean velocity) from a single dataset to apply the Bendat and Piersol (1986) run test, and we chose that each independent estimate is averaged over a 30-s period. This averaging period is consistent with the dominant turbulent length scales discussed later in the paper. Datasets for which we could not apply the run test and those found nonstationary at 5 min are excluded from further analysis. Stationary times of $\langle u'u' \rangle$ (Fig. 7a; Table 1) are chosen as averaging periods for all quantities throughout this paper with a median stationary time of 13 min. Since this period is longer than the stationary time of U_{ref}, this will contribute to uncertainty in a resulting mean flow.

3. Results

a. Flow conditions at the reference anemometer

In this section results from the reference anemometer are presented in order to characterize inflow conditions that will be used to interpret the flow field at the flight deck. Specifically, reference anemometer data are analyzed using the universal turbulence spectral model introduced by Kaimal et al. (1972). This model has been used and validated extensively for atmospheric surface layers over flat terrains (Kaimal and Finnigan 1994), the oceanic bottom boundary layer (Soulsby 1977; Trowbridge and Elgar 2003), at the air–sea interface (Gerbi et al. 2008), and in stratified oceanic flows by Scully et al. (2011). The spectral model for variances $\langle u'u' \rangle$, $\langle v'v' \rangle$, and $\langle w'w' \rangle$ is given by

$$\frac{kS_{\alpha\alpha}(k)}{\langle \alpha'^2 \rangle} = \frac{0.164(k/k_o)}{1 + 0.164(k/k_o)^{5/3}}, \tag{1}$$

where k is the streamwise wavenumber; $S_{\alpha\alpha}(k)$ is the measured velocity spectrum; α indicates the horizontal (u), vertical (w), or lateral (v) velocity component; $\langle \alpha'^2 \rangle$ is the velocity variance, and k_o is the wavenumber at which the peak of the variance preserving spectrum $kS_{\alpha\alpha}(k)$ occurs. Fitting this model to the measured anemometer spectrum gives estimates of the velocity variance $\langle \alpha'^2 \rangle$ and k_o. The peak of the variance-preserving spectrum occurs at the wavenumber $k = 2\pi/L_\alpha = 3.8k_o$ [given by Eq. (1)] from which the dominant energy containing length scale L_α can be calculated. Similarly, the Kaimal et al. (1972) universal cospectrum model for the surface layer of the atmospheric boundary layer is given as

$$\frac{kS_{w\alpha}(k)}{\langle w'\alpha' \rangle} = \frac{0.88(k/k_o)}{1 + 1.5(k/k_o)^{2.1}}, \tag{2}$$

where $S_{w\alpha}(k)$ is a real part of the measured cospectrum of the vertical velocity w and either horizontal velocity u or temperature T.

The procedure for calculating frequency spectra for each dataset is broken into three steps. First, instantaneous horizontal velocities (u and v) are rotated by the corresponding $\langle \beta \rangle$ such that mean lateral velocity $V_{\text{ref}} = 0$. Second, each continuous data segment goes through a 30-s high-pass filter. Third, data are divided into blocks of 512 points (25.6 s) with 50% overlap, spectra are calculated for each block, and spectra are averaged over all blocks. This procedure results in one spectrum for one continuous segment of data and the process is repeated for all available data segments within the stationary period. Then, the spectra from all continuous data segments are ensemble averaged to give a mean frequency spectrum for a dataset.

Wavenumber spectra $S_{\alpha\alpha}(k)$ and cospectra $S_{w\alpha}(k)$ are obtained by converting frequency scales to wavenumber scales using Taylor's frozen turbulence hypothesis, that is, $k = 2\pi f/U_{\text{ref}}$ and mean frequency spectra from the reference anemometer. Use of frozen turbulence hypothesis is considered valid for the shear-driven atmospheric surface layer (Kaimal et al. 1968), and effects of unsteady advection of turbulent eddies past the sensor are expected in the highly unstable surface layer characterized by free convection. This is further discussed in the next section.

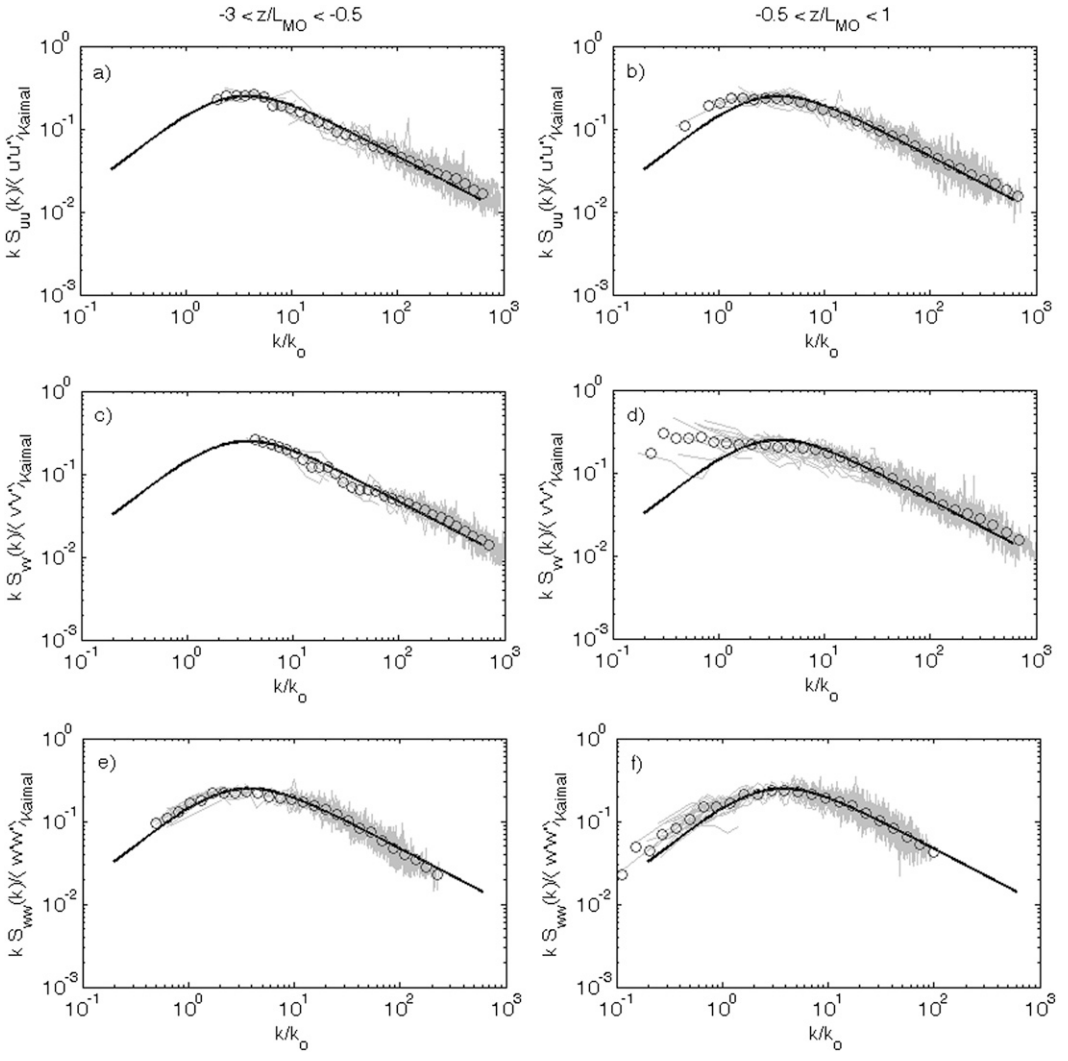

FIG. 8. Normalized observed wavenumber velocity spectra (light gray lines) conditionally sampled based on stability parameter z/L_{MO} vs nondimensional wavenumber k/k_o. (a),(b) Horizontal velocity spectra $S_{uu}(k)$; (c),(d) horizontal velocity spectra $S_{vv}(k)$; and (e),(f) vertical velocity spectra $S_{ww}(k)$. All spectra are normalized by their respective variances obtained from the fitting process to the Kaimal et al. (1972) model [Eq. (1)], shown by the thick black line. Circles indicate bin-averaged spectra.

Calculated wavenumber spectra and cospectra are then fitted to the Kaimal models using the two-parameter least squares fitting procedure similar to Gerbi et al. (2008) and Scully et al. (2011). To avoid possible contamination of the frequency spectra by ship motions, the spectra in a frequency band from $f = 0.1$–0.8 Hz are screened for contamination resulting from ship motions, and if found, a fixed range is excluded from the fitting process. The automatic screening process included finding the frequency of the maximum spectral peak, and if located in the 0.1–0.8-Hz frequency band, spectral energies within eight frequencies (four above and four below) of the spectral peak frequency are excluded, resulting in the removal of energy within the 0.313-Hz range centered on the maximum spectral peak. The 0.1–0.8-Hz frequency band was selected from the power spectra of concurrent ship's roll and pitch angle measurements by an IMU, and the 0.313-Hz range is selected based on the fact that ship motion contamination is primarily due to incident narrowbanded wind-driven waves with periods of 2–2.5 s, typical for the upper Chesapeake Bay area.

Fits of measured spectra to Kaimal models are shown in Fig. 8 for velocity variances, and in Fig. 9 for covariances $-\langle u'w'\rangle$ and $\langle w'T_S'\rangle$, where T_S is the anemometer sonic temperature. Spectra from all datasets are shown as light gray lines. Circles in each plot indicate spectral levels obtained by bin averaging spectral energy over logarithmically spaced k/k_o intervals over all spectra.

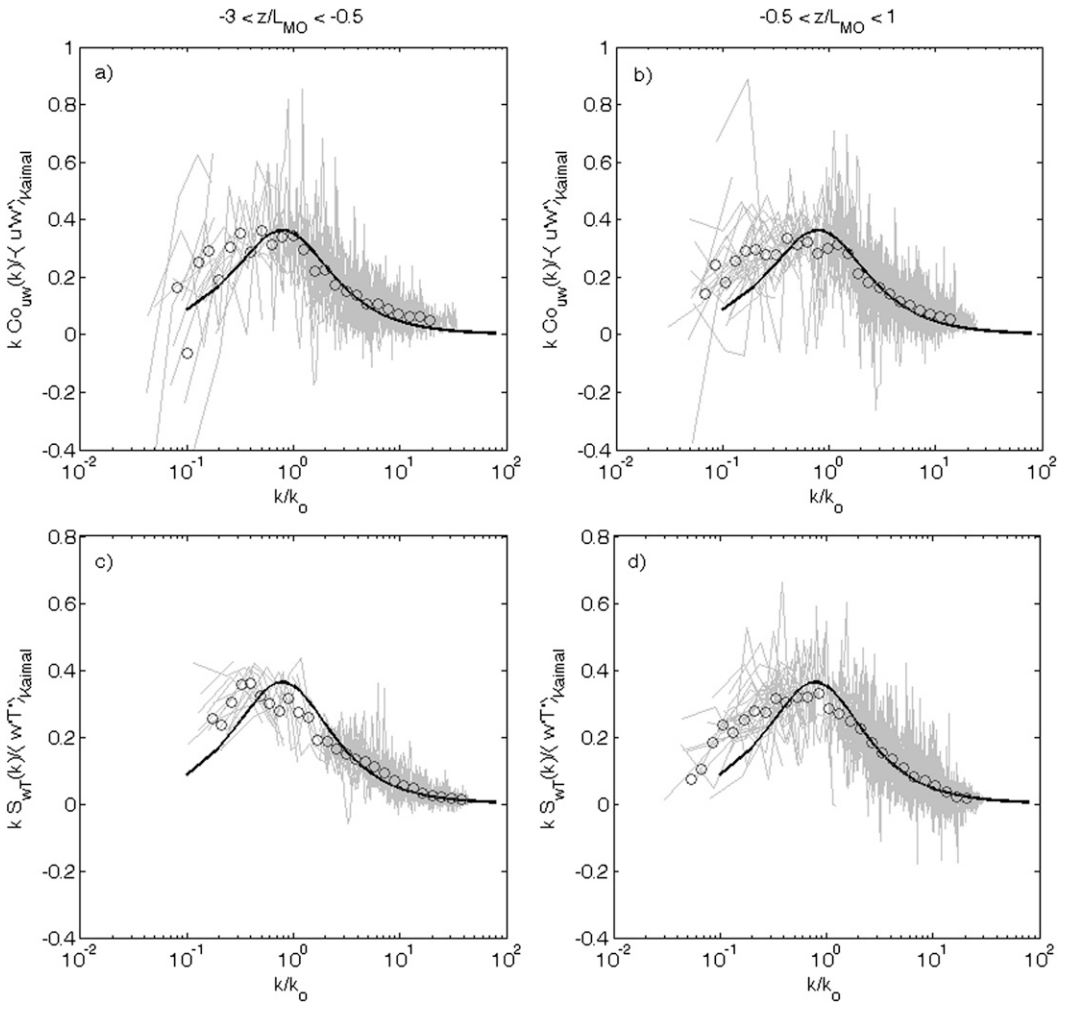

FIG. 9. Normalized observed wavenumber cospectra (light gray lines) conditionally sampled based on stability parameter z/L_{MO} vs nondimensional wavenumber k/k_o: (a),(b) $S_{uw}(k)$; (c),(d) $S_{wT}(k)$. All cospectra are normalized by their respective covariances obtained from the fitting process to the Kaimal et al. (1972) model [Eq. (2)], shown by the thick black line. Circles indicate bin-averaged spectra.

Spectra are further separated based on ratio z/L_{MO}, which is an indicator of stability in the surface layer (Kaimal and Finnigan 1994). Here, z is the elevation of the reference anemometer from the sea surface (see Figs. 1, 2) and L_{MO} is the Obukhov length calculated from anemometer data as

$$L_{\mathrm{MO}} = -\frac{u_*^3 \langle T_S \rangle}{g\kappa \langle w' T_S' \rangle_{\mathrm{Kaimal}}}, \tag{3}$$

where $\langle T_S \rangle$ is the mean sonic temperature, $\langle w' T_S' \rangle_{\mathrm{Kaimal}}$ is the covariance between vertical velocity and sonic temperature fluctuations obtained from the spectral fit, g is the gravitational acceleration, $\kappa = 0.41$ is the von Kármán constant, and the friction velocity u_* is approximated as $u_* \cong (-\langle u' w' \rangle_{\mathrm{Kaimal}})^{1/2}$. Negative L_{MO}, and hence negative z/L_{MO}, indicates unstable atmosphere and positive indicates stable atmospheric conditions. Over all datasets z/L_{MO} falls into a range from -3, indicating strongly unstable atmosphere, to $+1$, indicative of stable atmospheric conditions. We chose $z/L_{\mathrm{MO}} = -0.5$ as a separator between two distinct conditions based on the analysis below. Kaimal and Finnigan (1994) suggest that the spectrum of vertical velocity S_{ww} for unstable conditions shows insensitivity at large scales for $z/L_{\mathrm{MO}} < -0.3$; that is, k_o does not shift to lower wavenumbers with increasing instability. For our datasets, this is illustrated in Fig. 10, where length scale L_W derived from the S_{ww} spectrum fitted to Eq. (1) is plotted against z/L_{MO} for all datasets. A clear distinction occurs at $z/L_{\mathrm{MO}} \sim -0.5$, indicating that during unstable conditions, the dominant turbulent length scale associated with the peak energy

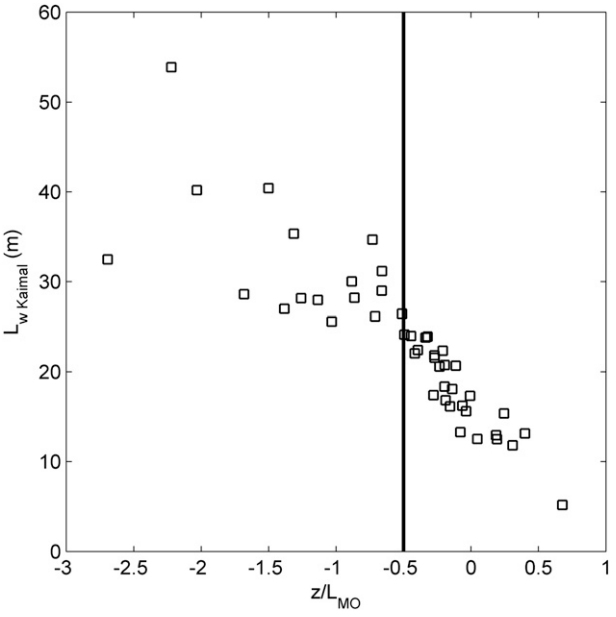

FIG. 10. Plot of length scale L_W derived from fitting vertical velocity spectra to the Kaimal et al. (1972) model [Eq. (1)] vs stability parameter z/L_{MO}. A clear change in L_W magnitudes occurs at $z/L_{MO} = -0.5$.

spectrum is not increasing with a decrease in stability. This is consistent with the notion that during strong unstable conditions, the nature of the turbulent flow changes from predominantly shear-driven turbulence during neutral stability to predominantly buoyancy-produced turbulence. For strongly stable conditions with $z/L_{MO} \sim 0.5$, turbulence is severely damped and consequently length scales of turbulence are reduced, as shown in Fig. 10 for L_W. Thus, all spectra that fall into the $-3 < z/L_{MO} < -0.5$ range are considered representative of the convective surface layer independent of stability, and spectra that fall into the $-0.5 < z/L_{MO} < 1$ range are considered representative of the shear-driven atmospheric boundary layer whose dominant energy containing length scale is highly dependent on the stability parameter z/L_{MO}.

Bin-averaged spectra in Fig. 8 show good agreement with the Kaimal model, both in locating spectral peaks and behavior at high wavenumbers. The low wavenumber range is not fully resolved for u and v spectra, although peaks clearly follow the Kaimal model. During the $-0.5 < z/L_{MO} < 1$ condition when the low wavenumber range is better resolved with our measurements, the largest deviation occurs in the horizontal velocity (v component) spectra shown in Fig. 8d, where the spectral peak is not present because of persistently high spectral energy for $k/k_o < 2$. We believe that this deviation from the Kaimal model at low wavenumbers can

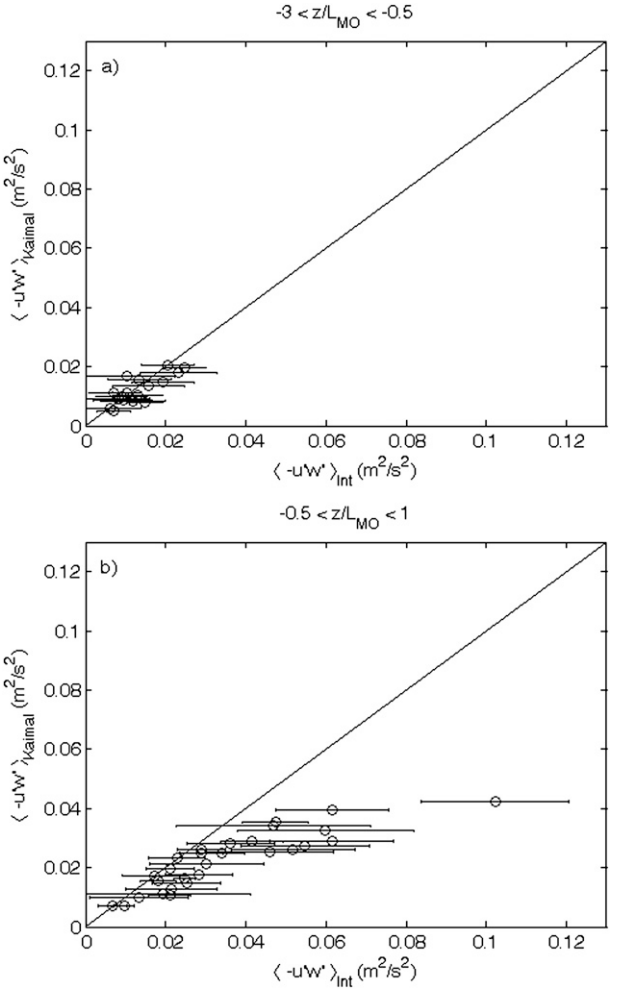

FIG. 11. Comparison of $-\langle u'w' \rangle_{Kaimal}$ and $-\langle u'w' \rangle_{Int}$ obtained from the integral of S_{uw} cospectra for (a) $-3 < z/L_{MO} < -0.5$ and (b) $-0.5 < z/L_{MO} < 1$. Horizontal lines indicate 95% confidence bands calculated using the bootstrap method (Efron and Gong 1983).

be attributed to unaccounted low-frequency ship maneuvers not removed with the 30-s high-pass filter. Bin-averaged cospectra shown in Fig. 9 agree well with the Kaimal cospectrum model given by Eq. (2) at high wavenumbers. Similarly as for variances, the deviations occur mostly at low wavenumbers, where observed cospectra are consistently greater than the model and the spectral peaks appear to be spread over a wider range of wavenumbers. There is no resolution discrepancy between strongly unstable and stable/unstable cospectra, suggesting that both shear stress $-\langle u'w' \rangle$ and buoyancy flux $\langle w'T_S' \rangle$ are well resolved in our measurements.

Figure 11 shows the comparison of $-\langle u'w' \rangle_{Kaimal}$ and $-\langle u'w' \rangle_{Int}$ obtained by integrating the S_{uw} cospectra over all frequencies. Error bars indicating 95% confidence bands of $-\langle u'w' \rangle_{Int}$ are also shown, calculated using the bootstrap method (Efron and Gong 1983) with

1000 bootstrap samples. Integral estimates are biased toward larger values, with 60% and 90% of the $-\langle u'w'\rangle_{\mathrm{Int}}$ data larger than $-\langle u'w'\rangle_{\mathrm{Kaimal}}$ for unstable and neutral/stable conditions, respectively. This bias is attributed to three factors. The first is bias due to flow distortion, as the presence of a moving ship alters the local characteristics of the atmospheric boundary layer and the full correspondence with Kaimal model is not expected from a reference anemometer, particularly at large scales. The second, as already mentioned, is bias introduced by unaccounted low-frequency ship maneuvers not removed with the 30-s-long high-pass filter. Contributions from these two factors can be clearly seen in Figs. 8 and 9. The third bias-contributing factor is the contamination of vertical and horizontal velocities by ship-induced motions and can be identified in Fig. 11 as data points with the largest departure from the 45° line. For those, statistical uncertainty in measurements of $-\langle u'w'\rangle_{\mathrm{Int}}$ does not explain the large discrepancy between the two estimates. For example, the largest value of $-\langle u'w'\rangle_{\mathrm{Int}}$ is $0.1\,\mathrm{m^2\,s^{-2}}$ (Fig. 11b), obtained during run 37, which correspond to the wind speed in excess of $10\,\mathrm{m\,s^{-1}}$ (see Fig. 4a) and significant wave height of 0.5 m discussed in the previous section. Clearly for this dataset $-\langle u'w'\rangle_{\mathrm{Int}}$ is contaminated by ship-induced motions by more than a factor of 2.5. In the analysis of flow behind the hangar superstructure that follows next, run 37 is not included, and based on Fig. 11b we estimate that turbulence stresses on the flight deck can be contaminated by ship motions by a factor of 2 at the most. This is a conservative estimate, as the ship motions are less pronounced at the flight deck in comparison to the bow anemometer.

To complete the picture of the atmospheric boundary layer conditions, Fig. 12 shows estimates of friction velocity $u_* = (\tau_S/\rho)^{1/2}$ (where τ_S is the wind shear stress at the sea surface and ρ is the air density) computed from $u_* \cong (-\langle u'w'\rangle_{\mathrm{Kaimal}})^{1/2}$ and independent estimates of u_* obtained from the Large and Pond (1981) model and Thomas Point meteorological station data when available. Results are comparable, following the same trends with z/L_{MO}, but they show a difference in magnitudes with reference anemometer u_* being consistently lower than the model estimates. This is expected since the anemometer estimate of u_* is approximated by the shear stress measured at an elevation of $z = 5.9$ m above sea surface, whereas u_* from the Large and Pond model is an estimate of friction velocity at the air–sea interface.

b. *Flow on the flight deck behind hangar superstructure*

In this section we present data from the stern anemometers. As mentioned in section 2, the basis for stern anemometer data selection and conditional sampling is based on the reference anemometer data. Not all datasets from stern anemometers are presented here. We focus on datasets along the centerline $y/H = 0$ and two off-centerline locations $y/H = \pm 0.6$ (see Fig. 5). As before, capital letters (e.g., U, V, and W) and terms in angle brackets indicate mean velocities and time averaging, respectively, over the same time periods for which the reference bow anemometer data are found stationary. Profiles of nondimensional mean velocities $U(x, y, z)/U_{\mathrm{ref}}$, $V(x, y, z)/U_{\mathrm{ref}}$, and $W(x, y, z)/U_{\mathrm{ref}}$ are shown in Fig. 13 as a function of z/H for nominal values of $x/H =$ 0.5, 1.0, 1.6, 2.1, 2.6, and 3.2. Data are segregated based on stability parameter, where full symbols indicate data that fall within $-3 < z/L_{\mathrm{MO}} < -0.5$ stability conditions, and open symbols are for data in the $-0.5 < z/L_{\mathrm{MO}} < 1$ range. Uncertainties of mean velocities and all quantities in this section are presented at the 95% confidence level calculated using the bootstrap method by Efron and Gong (1983) with 1000 bootstrap samples. The repeatability of trends in mean values is considered excellent although scatter is present. Profiles obtained under different stability criterion conditions seem to have the same shape and together they complement profiles, making them more continuous. Uncertainties are small, within 5%, and do not explain the scatter, which we believe can be attributed to the bias because of differences in mean yaw angles $\langle\beta\rangle$ among the datasets. For example, velocity profiles at $x/H = 2.1$ and $y/H = -0.6$ (open triangles) are clearly different from other measurements at this location. For these datasets $\langle\beta\rangle$ ranges between positive 4° and 6° and corresponds to the largest deviation in the mean yaw angle (see Fig. 6). This implies

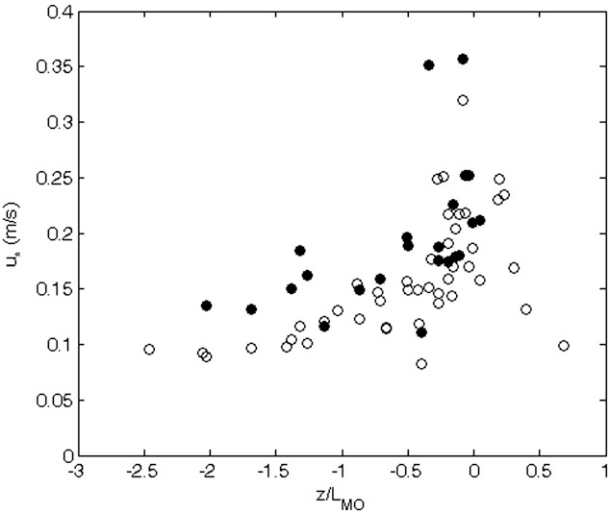

FIG. 12. Friction velocity u_* vs stability parameter z/L_{MO} for estimate of u_* from Large and Pond (1981) model (filled circles) and $u_* \cong (-\langle u'w'\rangle_{\mathrm{Kaimal}})^{1/2}$ (open circles).

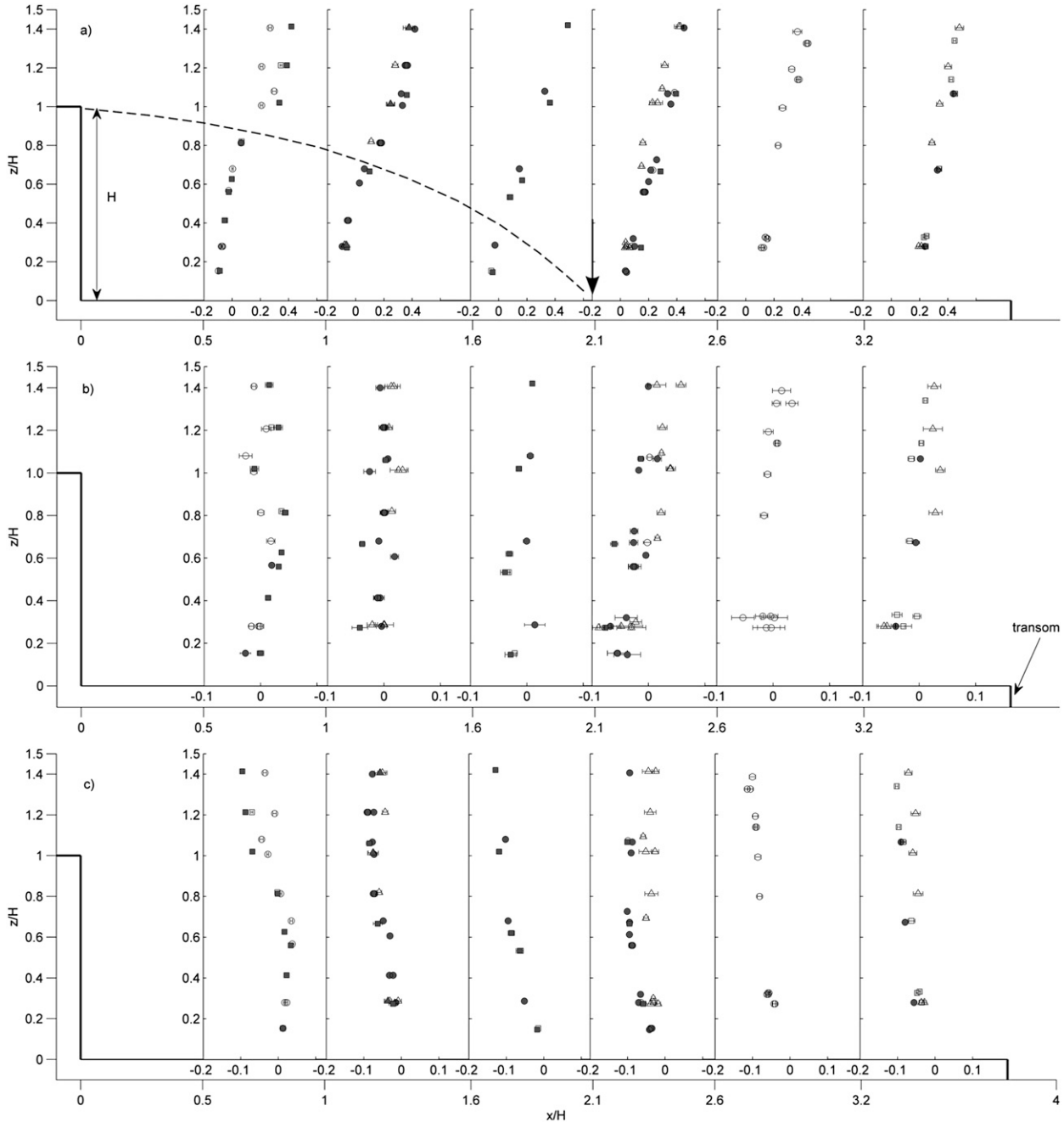

FIG. 13. Profiles of nondimensional mean flow for (a) U/U_{ref}, (b) V/U_{ref}, and (c) W/U_{ref} with $y/H = 0$ (circles), $y/H = 0.6$ (squares), and $y/H = -0.6$ (triangles) using filled symbols for $-3 < z/L_{\mathrm{MO}} < -0.5$ and open symbols for $-0.5 < z/L_{\mathrm{MO}} < 1$. Hangar height H is 1.5 m. In (a), the dashed line indicates approximate boundary of the separated recirculating flow and the arrow indicates approximate location of the reattachment point.

that the wind is coming from the port side and presumably exposing the flight deck anemometers (located at 0.6 H from the centerline on the port side) to the incoming wind free of superstructure obstruction. As a result U, V, and W profiles have different trends, where U velocity is reduced in magnitude and V is increased, as expected if the flow is coming at an increasing yaw angle.

Profiles are consistent with what one would expect in the flow field behind a backward-facing step. At station $x/H = 0.5$, the U magnitude is negative and about $z/H = 0.8$ profile exhibits an inflection. Downstream at station

$x/H = 2.1$, U shows no reverse flow up to the lowest measurement location of $z/H = 0.13$. The maximum negative U velocity is 10% of U_{ref}, comparable to measurements in the recirculation zone behind 3D rectangular blocks (Angelinchaab and Tachie 2008) and a backward-facing step (Eaton and Johnston 1981). Further downstream at stations $x/H = 2.6$ and 3.2, U increases monotonically with z/H and reaches about 50% of U_{ref}. Mean vertical velocity W also exhibits inflection points at $x/H = 0.5$ and $z/H = 0.8$, where its magnitude changes from slightly positive to negative and reaches 10% of U_{ref} at the highest measurement location. For the rest of the profiles, W is negative and reduces in magnitude with decreasing z/H as expected, as it needs to vanish at the wall. Lateral mean velocity V is rarely reported in the literature and is shown in Fig. 13b for completeness. Lateral velocities are found to be small and typically less than 10% of U_{ref} and show no significant variation with elevation.

A combination of U and W profiles illustrates the formation of a recirculation region downstream of the hangar superstructure. Within the spatial resolution of the present measurements, we estimate the flow reattachment point at $x/H = 2.1$ on the basis that U is virtually zero there at the lowest measurement location (see Fig. 13a). This estimate of reattachment location is consistent with observations from Miklosovic et al. (2011) in the wind tunnel from measurements on a 4% geometrical model of the YP. Tinney and Ukeiley (2009) report the same reattachment location for a flow over the double-backward step, where the second step represents the stern transom. Thus, profiles at stations $x/H =$ 0.5–2.1 are considered to be in the recirculation region, while profiles at stations $x/H = 2.6$–3.2 are in the recovery region.

Turbulence statistics of stern anemometers are calculated by integrating spectra over all frequencies and are indicated without subscripts. Profiles of normalized turbulence intensities $\langle u'u'\rangle^{1/2}/U_{ref}$, $\langle v'v'\rangle^{1/2}/U_{ref}$, and $\langle w'w'\rangle^{1/2}/U_{ref}$, and associated uncertainties are shown in Fig. 14. Quantitatively, magnitudes are consistent with the backward-facing step results of Eaton and Johnston (1981) and Etheridge and Kemp (1978) and range between 5% and 15% of U_{ref} and have a slightly increasing trend with z/H. We do not observe a significant increase in $\langle v'v'\rangle^{1/2}/U_{ref}$ and $\langle w'w'\rangle^{1/2}/U_{ref}$ turbulence intensities downstream of the reattachment point, as observed by Tinney and Ukeiley (2009). One possible explanation for not observing this in our datasets is the difference in geometry between their wind tunnel model and the present ship. On the YP, there is a significant superstructure upstream of hangar step, including the pilot house. For headwind, the flow moving over the top of the hangar already has residual turbulence from being in the wake of the pilot house and explains the reason why our turbulence intensities show very little variation with elevation above the flight deck (Brownell et al. 2012).

Figure 15 shows profiles of the correlation coefficient $K = -\langle u'w'\rangle/(\langle u'u'\rangle^{1/2}\langle w'w'\rangle^{1/2})$ and ratios $\langle w'w'\rangle/\langle u'u'\rangle$ and $\langle v'v'\rangle/\langle u'u'\rangle$. The correlation coefficient K is considered as an indicator of the efficiency of vertical momentum transport. At station $x/H = 1.0$, a peak occurs in the K profile at a value of $z/H = 0.8$, consistent with the position of inflection in the U profile. This peak (K_{max}) is still visible downstream at $x/H = 1.6$, and by $x/H = 2.1$ the profile has become fuller in the vicinity of the peak. At stations $x/H = 2.6$ and 3.2, K_{max} is no longer noticeable, with K approximately constant and equal to 0.45–0.5 for points above $z/H \sim 0.25$. For profiles with a peak in the correlation coefficient, K_{max} is assumed to signify the center of the shear layer on the flight deck. Furthermore, K values above the peaks are approximately equal to 0.4–0.5, suggesting that this value may represent the outer edge of the shear layer. If this conjecture is valid, then the upper boundary of the shear layer in the recovery region lies near $z/H \sim 0.25$, the lower bound of the measurement domain for stations $x/H = 2.6$ and 3.2. The values of $K = 0.4$–0.5 in the outer part of the flow above the shear layer are in good agreement with Etheridge and Kemp (1978), who obtained $K = 0.55$ in the outer part of the shear layer behind a 2D rearward-facing step. K_{max} values are similar in magnitude to those observed in a plane mixing layer of $K = 0.6$ by Townsend (1956). On the inner side of the K_{max}, the correlation coefficient ranges from 0.1 at $x/H = 0.5$ to 0.4 at $x/H = 1.6$.

Variations of $\langle w'w'\rangle/\langle u'u'\rangle$ and $\langle v'v'\rangle/\langle u'u'\rangle$ with z/H are particularly significant in the recirculation region ($x/H = 0.5$–2.1). At $x/H = 1.0$ and $z/H = 0.25$, for example, $\langle w'w'\rangle/\langle u'u'\rangle$ reaches 1.1 in the center of the shear layer and above it is approximately 0.5, consistent with the classical plane mixing layer (Townsend 1956) and the value obtained in the turbulent shear layer behind a backward-facing step (Castro and Haque 1987). Trends in $\langle v'v'\rangle/\langle u'u'\rangle$ in the recirculation zone are similar to $\langle w'w'\rangle/\langle u'u'\rangle$ but with large magnitudes at the lowest measurement location and reach value of 1.5, consistent with Castro and Haque (1987).

4. Conclusions

This paper presents details of a new and unique facility for systematic measurement of in situ velocities in the near wake of a ship's superstructure, and it discusses in detail a set of experiments conducted under a headwind condition while underway in the Chesapeake Bay.

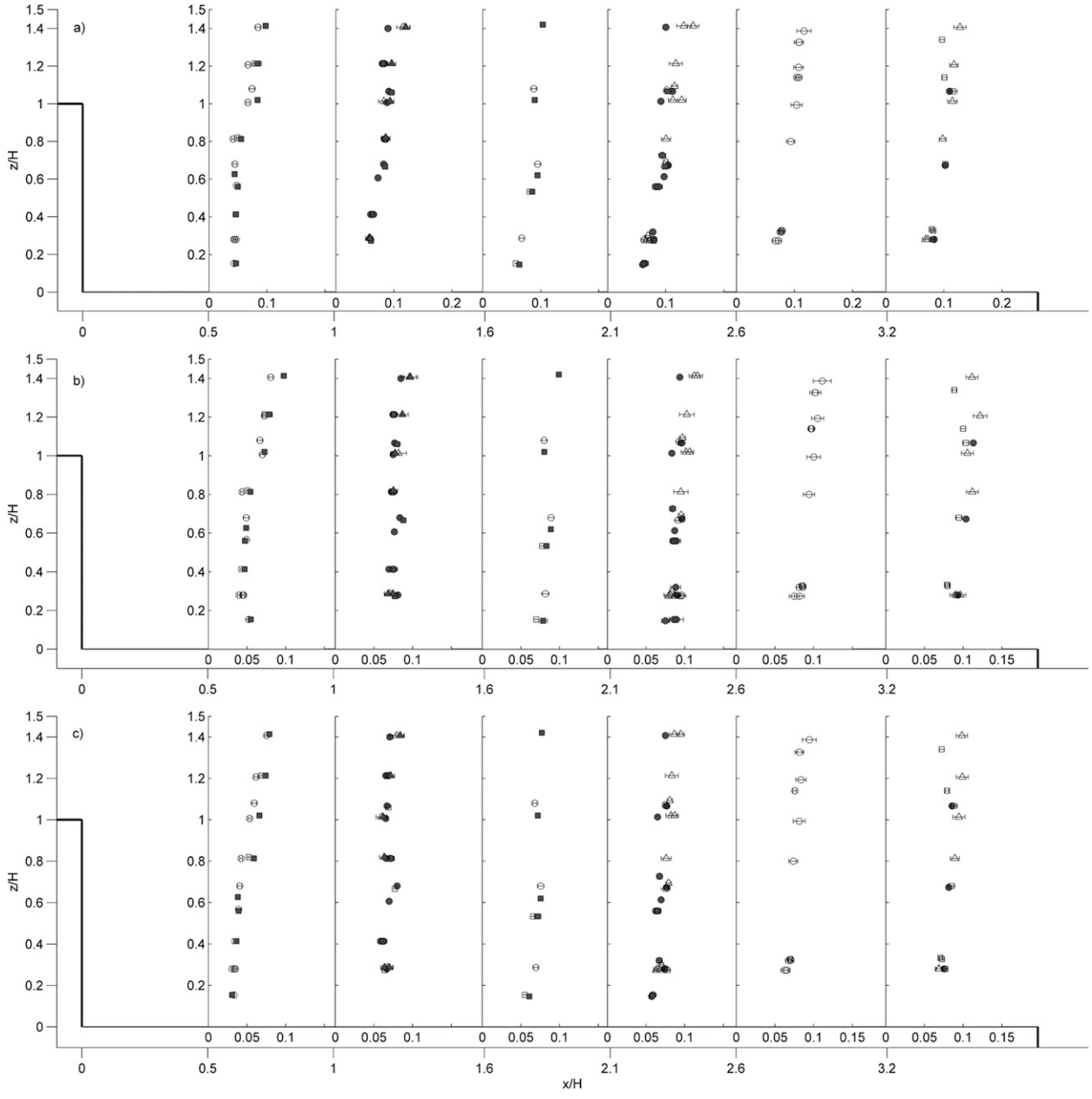

FIG. 14. Profiles of turbulence intensities (a) $\langle u'u' \rangle^{1/2}/U_{\text{ref}}$, (b) $\langle v'v' \rangle^{1/2}/U_{\text{ref}}$, and (c) $\langle w'w' \rangle^{1/2}/U_{\text{ref}}$. Symbols as in Fig. 13.

Environmental conditions encountered during a 1-yr period over which these experiments were conducted can be qualified as moderate with typical wind speeds from 2 to 10 m s^{-1} and wind-generated waves with an approximately 2.5-s period. It is shown that under these conditions, stationarity of measured data—that is, periods of essentially steady flow—can be obtained in a range from 5 to 30 min.

With the present instrumentation setup and during stationary periods, all relevant scales in the flow that contribute to the variances of turbulent fluctuations can be resolved. Reference anemometer spectra and cospectra have the same general form, when properly scaled, as the established universal Kaimal spectra from a surface region of an atmospheric boundary layer. These results are particularly encouraging, so methods are currently being developed for measuring the near-surface atmospheric boundary layer using the same ship but with a modified bow mount to accommodate an array of eight vertically stacked anemometers.

Conditional sampling of the mean flow and turbulence statistics of the flight deck anemometers based on the

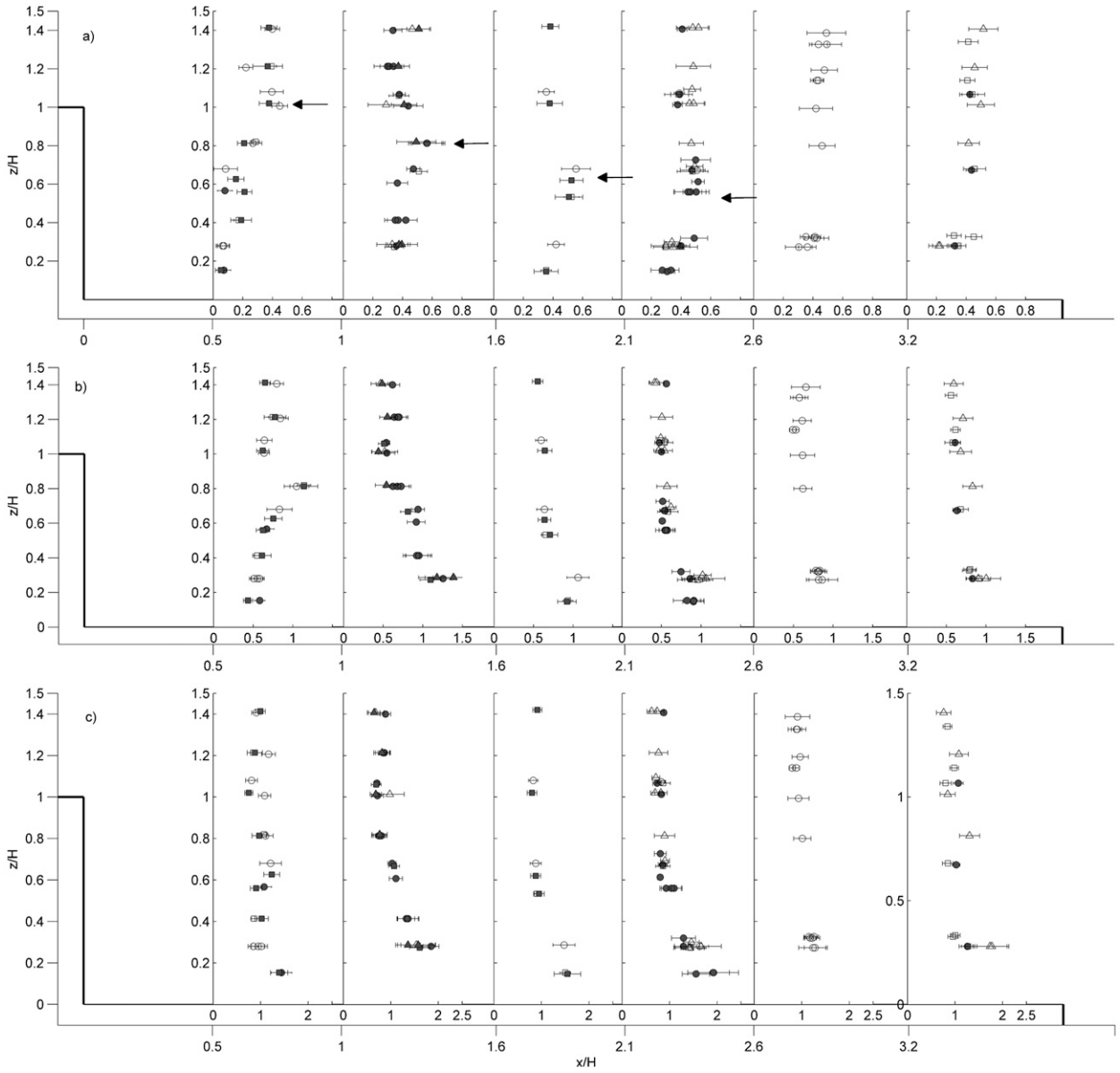

FIG. 15. (a) Shear correlation coefficient $K = -\langle u'w'\rangle/\sigma_u\sigma_w$, (b) $\langle w'w'\rangle/\langle u'u'\rangle$, and (c) $\langle v'v'\rangle/\langle u'u'\rangle$. Symbols as in Fig. 13. Arrows in (a) indicate locations of K_{max}.

stability parameter z/L_{MO} shows no statistically significant variations between the convectively driven and shear-driven atmospheric surface layer. A plausible explanation is that turbulent eddies present in the flow during different atmospheric conditions with length scales shown in Fig. 10 get broken down in the wake of the ship superstructure well upstream, and as a result separated flow downstream of the hangar is insensitive to the inflow conditions, as observed from the reference anemometer.

For the headwind conditions, the structure of the separated flow behind the hangar superstructure closely resembles the flow behind a backward-facing step and measured turbulence statistics are consistent with the published data. These conclusions suggest that applicability and fidelity of current air-wake models can be validated for headwind conditions and hangar/flight deck geometry and the results compared to the substantial body of literature existing on the flows over the backward-facing step.

The observed location of the present reattachment point on the flight deck is consistent with Tinney and Ukeiley's (2009) measurements with similar geometry and Miklosovic et al.'s (2011) measurements on the

scaled model of the YP vessel. Both of these studies were obtained in wind tunnels with no imposed boundary layer profile. Eaton and Johnston (1981) concluded that the inflow boundary layer has a weak effect on the reattachment location, provided that the ratio of boundary layer thickness δ to hangar height is very large. Our measurements fit that criteria and suggest that inclusion of the atmospheric boundary layer in the validations of models for a headwind condition is not necessary. However, the flow structure in the near wake changes drastically with the direction of the wind over deck (Polsky 2003) and air-wake models need to capture these changes. For those conditions the influence of the incoming atmospheric boundary layer needs to be studied systematically. Recent work at the United States Naval Academy included data collection over a range of wind over deck conditions and the results will be the subject of future publications.

Acknowledgments. This project is funded by the Office of Naval Research through the Young Investigator Program (PI: Murray R. Snyder). We would like to recognize the invaluable contributions of John Burks, Collin Wilkinson, and Joshua Shishkoff to this paper and to the USNA ship air wake program. We are also grateful to the crew of YP676 for their invaluable assistance during data collection.

REFERENCES

Angelinchaab, M., and M. F. Tachie, 2008: PIV study of separated and reattached open channel flow over surface mounted blocks. *J. Fluids Eng.,* **130,** 061206, doi:10.1115/1.2911677.

Bendat, J. S., and A. G. Piersol, 1986: *Random Data: Analysis and Measurement Procedures.* Wiley & Sons, Inc., 566 pp.

Brooks, I., 2008: Spatially distributed measurements of platform motion for the correction of ship-based turbulent fluxes. *J. Atmos. Oceanic Technol.,* **25,** 2007–2017.

Brownell, C. J., L. Luznik, M. R. Snyder, H. S. Kang, and C. H. Wilkinson, 2012: In situ velocity measurements behind ship superstructure. *J. Aircr.,* **49,** 1440–1450.

Bunnell, J. W., 2001: An integrated time-varying airwake in a UH-60 Black Hawk shipboard landing simulation. *Proc. AIAA Modeling and Simulation Technologies Conf. and Exhibit,* Montreal, QC, Canada, AIAA, Paper AIAA 2001-4065. [Available online at http://www.aviationsystems.arc.nasa.gov/publications/hitl/technical/2001_4065.pdf.]

Castro, I. P., and A. Haque, 1987: The structure of turbulent shear layer bounding a separation region. *J. Fluid Mech.,* **179,** 439–468.

Eaton, J. K., and J. P. Johnston, 1981: A review of research on subsonic turbulent flow reattachment. *AIAA J.,* **19,** 1093–1100.

Efron, B., and G. Gong, 1983: A leisurely look at the bootstrap, the jackknife and cross-validation. *Amer. Stat.,* **37,** 36–48.

Etheridge, D. W., and P. H. Kemp, 1978: Measurements of turbulent flow downstream of a rearward-facing step. *J. Fluid Mech.,* **86,** 545–566.

Gerbi, G., J. H. Trowbridge, J. B. Edson, A. L. Plueddemann, E. A. Terray, and J. J. Fredericks, 2008: Measurements of momentum and heat transfer across the air–sea interface. *J. Phys. Oceanogr.,* **38,** 1054–1071.

Healey, J. V., 1987: The prospects for simulating the helicopter/ship interface. *Nav. Eng. J.,* **99,** 45–63.

——, 1992: Establishing a database for flight in the wakes of structures. *J. Aircr.,* **29,** 559–564.

Kaimal, J. C., and J. J. Finnigan, 1994: *Atmospheric Boundary Layer Flows: Their Structure and Measurements.* Oxford University Press, 289 pp.

——, J. C. Wyngaard, and D. A. Haugen, 1968: Deriving power spectra from a three-component sonic anemometer. *J. Appl. Meteor.,* **7,** 827–837.

——, ——, Y. Izumi, and O. R. Cote, 1972: Spectral characteristics of surface-layer turbulence. *Quart. J. Roy. Meteor. Soc.,* **98,** 563–589.

Large, W. G., and S. Pond, 1981: Open ocean momentum flux measurements in moderate to strong winds. *J. Phys. Oceanogr.,* **11,** 324–336.

Lin, W. Q., L. P. Sanford, S. E. Suttles, and R. Valigura, 2002: Drag coefficients with fetch-limited wind waves. *J. Phys. Oceanogr.,* **32,** 3058–3074.

Luznik, L., and K. A. Flack, 2010: Observations of turbulent flow fields in the Chesapeake Bay estuary for tidal energy conversion. *Proc. Oceans '10 MTS/IEEE Seattle,* Seattle, WA, MTS and IEEE, doi:10.1109/OCEANS.2010.5664375.

Miklosovic, D. S., M. R. Snyder, and H. S. Kang, 2011: Ship air wake wind tunnel test results. *Proc. 29th AIAA Applied Aerodynamic Conf.,* Honolulu, Hawaii, AIAA, Paper AIAA 2011-3155, doi:10.2514/6.2011-3155.

Miller, S. D., T. S. Hristov, J. B. Edson, and C. A. Friehe, 2008: Platform motion effects on measurements of turbulence and air–sea exchange over the open ocean. *J. Atmos. Oceanic Technol.,* **25,** 1683–1694.

Polsky, S. A., 2003: CFD prediction of airwake flowfields for ships experiencing beam winds. *Proc. 21st AIAA Applied Aerodynamics Conf.,* Orlando, FL, AIAA, Paper AIAA 2003-3657, doi:10.2514/6.2003-3657.

——, and C. W. S. Bruner, 2000: Time-accurate computational simulations of an LHA ship airwake. *Proc. 18th Applied Aerodynamics Conf.,* Denver, CO, AIAA, Paper AAAA-2000-4126. [Available online at http://arc.aiaa.org/doi/abs/10.2514/6.2000-4126.]

Scully, M. E., W. R. Geyer, and J. H. Trowbridge, 2011: The influence of stratification and nonlocal turbulent production on estuarine turbulence: An assessment of turbulence closure with field observations. *J. Phys. Oceanogr.,* **41,** 166–185.

Snyder, M. R., H. S. Kang, C. J. Brownell, L. Luznik, D. S. Miklosovic, J. S. Burks, and C. H. Wilkinson, 2011: USNA ship air wake program overview. *Proc. 29th AIAA Applied Aerodynamic Conf.,* Honolulu, Hawaii, AIAA, Paper AIAA 2011-3153, doi:10.2514/6.2011-3153.

Soulsby, R. L., 1977: Similarity scaling of turbulence spectra in marine and atmospheric boundary layers. *J. Phys. Oceanogr.,* **7,** 934–937.

——, 1980: Selecting record length and digitization rate for near-bed turbulence measurements. *J. Phys. Oceanogr.,* **10,** 208–219.

Tinney, C. E., and L. S. Ukeiley, 2009: A study of a 3-D double backward-facing step. *Exp. Fluids,* **47,** 427–438.

Townsend, A. A., 1956: *The Structure of Turbulent Shear Flow.* Cambridge University Press, 442 pp.

Trowbridge, J., and S. Elgar, 2003: Spatial scales of stress-carrying nearshore turbulence. *J. Phys. Oceanogr.,* **33,** 1122–1128.

Wilkinson, C. H., S. J. Zan, N. E. Gilbert, and J. D. Funk, 1999: Modelling and simulation of ship air wakes for helicopter operations—A collaborative venture. Symposium on fluid dynamics problems of vehicles operating near or in the air-sea interface, NATO Science and Technology Organization Rep. RTO-MP-015, 8-1–8-12. [Available online at http://ftp.rta.nato.int/public//PubFullText/RTO/MP/RTO-MP-015///$MP-015-08.PDF.]

Zan, S. J., G. F. Syms, and B. T. Cheney, 1999: Analysis of patrol frigate air wakes. Symposium on fluid dynamics problems of vehicles operating near or in the air-sea interface, NATO Science and Technology Organization Rep. RTO-MP-015, 7-1–7-14. [Available online at http://ftp.rta.nato.int/public//PubFullText/RTO/MP/RTO-MP-015///$MP-015-07.PDF.]